The Astrophysical Journal, 864:18 (13pp), 2018 September 1 https://doi.org/10.3847/1538-4357/aad3b4

A Data-constrained Model for Coronal Mass Ejections Using the Graduated Cylindrical Shell Method

T. Singh[1], M. S. Yalim[2], and N. V. Pogorelov[1,2]
[1] Department of Space Science, The University of Alabama in Huntsville, AL 35805, USA; talwinder.singh@uah.edu
[2] Center for Space Plasma and Aeronomic Research, The University of Alabama in Huntsville, AL 35805, USA
Received 2018 January 10; revised 2018 June 18; accepted 2018 July 13; published 2018 August 27

Abstract

Coronal mass ejections (CMEs) are major drivers of extreme space weather conditions, as this is a matter of serious concern for our modern technologically dependent society. The development of numerical approaches that would simulate CME generation and propagation through the interplanetary space is an important step toward our capability to predict CME arrival times at Earth and their geoeffectiveness. In this paper, we utilize a data-constrained Gibson–Low (GL) flux rope model to generate CMEs. We derive the geometry of the initial GL flux rope using the graduated cylindrical shell method. This method uses multiple viewpoints from *STEREO A* and *B* Cor1/Cor2, and *Solar and Heliospheric Observatory* (*SOHO*)/LASCO C2/C3 coronagraphs to determine the size and orientation of a CME flux rope as it starts to erupt from the Sun. A flux rope generated in this way is inserted into a quasi-steady global magnetohydrodynamics (MHD) background solar wind flow driven by *Solar Dynamics Observatory*/Helioseismic and Magnetic Imager line-of-sight magnetogram data, and erupts immediately. Numerical results obtained with the Multi-Scale Fluid-Kinetic Simulation Suite (MS-FLUKSS) code are compared with *STEREO* and *SOHO*/LASCO coronagraph observations, in particular in terms of the CME speed, acceleration, and magnetic field structure.

Key words: magnetohydrodynamics (MHD) – methods: data analysis – methods: numerical – solar wind – Sun: corona – Sun: coronal mass ejections (CMEs)

1. Introduction

Coronal mass ejections (CMEs) are the most energetic events in our solar system. They are large structures of plasma confined in a sheared/twisted magnetic field being ejected from the low solar corona. Generally, they originate from the magnetically active regions of the Sun. With ejected mass reaching 10^{12} kg and speeds up to 3000 km s^{-1}, they carry a huge amount of kinetic and magnetic energy (Chen 2011). A CME directed toward Earth can cause extreme space weather conditions that affect space-borne and ground-based technological systems. Therefore, predicting the CME eruption, its arrival time at Earth, and its possible impact on it are of great importance to our technologically advanced society. Many past and present observatories and instruments (both space-borne and ground-based) have helped us understand the Sun–Earth connection. A number of CME arrival time models have been proposed over the years. They include empirical models (e.g., Vandas et al. 1996; Brueckner et al. 1998; Wang et al. 2002; Manoharan et al. 2004; Gopalswamy et al. 2005), drag-based models used to predict CME arrival times (Vrsnak 2001; Vrsnak & Gopalswamy 2002), and such physics-based models as, e.g., shock time of arrival (STOA), STOA-2 (Moon et al. 2002).

Substantial success has been achieved in numerical modeling of CMEs (e.g. Mikic & Linker 1994; Forbes & Priest 1995; Linker & Mikic 1995; Gibson & Low 1998; Antiochos et al. 1999; Titov & Demoulin 1999; Lin & Forbes 2000; Hu 2001; Moore et al. 2001; Torok et al. 2004; Chane et al. 2005; Torok & Kliem 2005; Forbes et al. 2006; Jacobs et al. 2006; Kliem & Torok 2006; Fan & Gibson 2007; Aulanier et al. 2010; Amari et al. 2011, 2014; Chen 2011; Roussev et al. 2012; Titov et al. 2014; Schmieder et al. 2015; Jiang et al. 2016; Jin et al. 2017a; Lugaz et al. 2017) and their propagation into the inner heliosphere (e.g. Odstrcil & Pizzo 1999, 2009; Riley et al. 2003, 2015a, 2015b; Roussev et al. 2003; Manchester et al. 2006; Usmanov & Goldstein 2006; Lionello et al. 2009, 2016; Wu et al. 2009; Detman et al. 2011; Feng et al. 2011, 2015; Lugaz & Roussev 2011; Usmanov et al. 2011; Wang et al. 2011; Intriligator et al. 2012; Hayashi 2013; Riley & Richardson 2013; Sokolov et al. 2013; Leake et al. 2014; Lee et al. 2014; van der Holst et al. 2014; Oran et al. 2015; Linker et al. 2016; Merkin et al. 2016).

Previous CME models such as the blob model and over-pressured spherical plasmoid (e.g., Chane et al. 2005; Odstrcil & Pizzo 1999) do not take into consideration the magnetic field inside a CME. These approaches do not give us a complete picture of CME propagation because the conversion from magnetic to kinetic energy is an integral part of this phenomenon. Processes like CME–CME collisions in the interplanetary space rely heavily on the CME magnetic field. Thus, the above models fail to simulate the full complexity of CME events (Shen et al. 2017). The magnetic field produced by a CME is one of the critical parameters determining its geoeffectiveness, i.e., the ability to disturb Earth's magnetosphere and upper atmosphere. CMEs with a negative z-component of the magnetic field vector, B_z, have been observed to be more geoeffective due to coupling with the positive B_z of Earth's magnetosphere, where the z-axis is perpendicular to the solar ecliptic plane (Lockwood et al. 2016). Thus, CME models that ignore such magnetic structure can hardly be used to predict their geoeffectiveness.

In this paper, we use a Gibson–Low (GL) type flux rope model (Gibson & Low 1998) to simulate a CME. Similar models have previously been applied by, e.g., Manchester et al. (2004a, 2004b, 2006, 2014a, 2014b), Jin et al. (2016, 2017a, 2017b), Kataoka et al. (2009), Lugaz et al. (2005, 2007), Poedts & Pomoell (2017), Pomoell et al. (2017), and Shiota & Kataoka (2016). Jin et al. (2017b) describe a data-constrained CME model to find the GL flux rope parameters from observations. They use

the size of neutral line in the source active region to find the GL size parameters. The GL magnetic field strength is found indirectly from a parametric study.

In the present paper, we acquire the GL flux rope size parameters directly from coronagraph observations of a CME by using the Graduated Cylindrical Shell (GCS) method (Thernisien et al. 2006). Afterward, a parametric study is performed to compute the magnetic field strength of flux rope indirectly. This method is described in detail in Section 2.

This approach is complementary to the CME model of Jin et al. (2017b). It allows us to determine the initial flux rope geometry more accurately, because we do not impose excessive energy in the initial flux rope configuration thereby avoiding its excessive heating and acceleration. Moreover, our method of determining the GL flux rope parameters from the observational data can be automatized by a user-friendly graphical user interface (GUI) similar to the Eruptive Event Generator (EEGGL; Gibson and Low 1998; Borovikov et al. 2017) in the Community Coordinated Modeling Center. While complex CME models involving an energy buildup before eruption (e.g., Titov & Demoulin 1999; Amari et al. 2014) exist, our model implements a rather simple, but data-driven, eruption mechanism triggered by the force imbalance between the initial flux rope and the surrounding background solar wind as soon as the flux rope is inserted. As compared with a number of CME initiation models described in the reviews of Chen (2011) and Aulanier (2014), especially taking into account existing limitations on data-driven models, our approach is computationally more efficient and provides a practical alternative for operational space weather forecasting.

We have implemented this CME model as a module in the Multi-Scale Fluid-Kinetic Simulation Suite (MS-FLUKSS; Pogorelov et al. 2014), a suite of adaptive mesh refinement (AMR) codes designed to solve the coupled system of magnetohydrodynamics (MHD), gas dynamics Euler, and kinetic Boltzmann equations (Borovikov et al. 2009, 2013; Pogorelov et al. 2009, 2013). MS-FLUKSS is built upon the Chombo AMR framework (Colella et al. 2007). It also has modules that treat pickup ions either kinetically or as a separate fluid, and turbulence models applicable beyond the Alfvénic surface (Gamayunov et al. 2012; Kryukov et al. 2012; Adhikari et al. 2015).

Previously, we have studied a number of CME events generated by the blob model (Chane et al. 2005) in the inner heliosphere using MS-FLUKSS (Pogorelov et al. 2017). Our present CME model employs a newly developed, data-driven MHD global solar corona model (Yalim et al. 2017).

The structure of the paper is as follows. In Section 2, we present an overview of our global solar corona and CME models. In Section 3, we present our numerical results. Finally, in Section 4, we draw some conclusions pertinent to our simulations.

2. Models

2.1. Global Solar Corona Model

There have been a few attempts to obtain flux ropes in solar corona suitable for CME generation. Worth mentioning, in particular, is the magnetofrictional method (Cheung et al. 2015; Fisher et al. 2015). Jiang et al. (2016) reported a CME born at an active region on the solar surface on the basis of the MHD conservation laws with appropriate plasma heating mechanism similar to the one used in this paper. We are also pursuing similar approaches. However, they have been applied so far only to localized active regions. The difficulty is to ensure that such structures create CMEs only when they are observed. A simplified alternative is to insert a flux rope defined by analytical solutions into a previously obtained, background solar wind flow propagating toward Earth. This imposes critical restrictions onto any background model, as otherwise even a perfect CME model may lead to inaccurate results. On the other hand, oversimplified models of CME propagation may show excellent agreement with observed CME shock arrival time at Earth when they propagate through the background solar wind, which disagrees with in situ observations during quiet-Sun periods.

For this reason, we have developed a new, data-driven global MHD model of solar corona and inner heliosphere (Yalim et al. 2017), which is based on vector magnetograms, and therefore makes it possible to implement mathematically consistent, characteristics-based boundary conditions. As we are solving the system of hyperbolic MHD equations, the boundary conditions in lower corona should be specified according to the theory of characteristics.

Consider for simplicity a 1D system of conservation laws:

$$\frac{\partial \boldsymbol{U}}{\partial t} + \frac{\partial \boldsymbol{F}}{\partial x} = 0, \tag{1}$$

where $\boldsymbol{U}$ and $\boldsymbol{F}$ are the vectors of conservative variables and corresponding fluxes, respectively.

This system can be rewritten in a quasi-linear form as

$$\frac{\partial \boldsymbol{U}}{\partial t} + A\frac{\partial \boldsymbol{U}}{\partial x} = 0, \quad A = \frac{\partial \boldsymbol{F}}{\partial \boldsymbol{U}}. \tag{2}$$

Because the MHD system is hyperbolic, the Jacobian matrix, A, has only real eigenvalues, λ_i, $i = 1, \ldots, 8$. Moreover, there exists a non-degenerate, complete set of left and right eigenvectors for this matrix, i.e.,

$$A\Omega_{\mathrm{R}} = \Lambda\Omega_{\mathrm{R}}, \quad \Omega_{\mathrm{L}}A = \Lambda\Omega_{\mathrm{L}}, \tag{3}$$

where Ω_{R} and Ω_{L} are the matrices formed by the right and left eigenvectors of A, used as columns and rows, respectively. In addition, Λ is a diagonal matrix formed of eigenvalues of A.

From the above, it follows that

$$A = \Omega_{\mathrm{R}}\Lambda\Omega_{\mathrm{L}}. \tag{4}$$

On introducing the vector $\boldsymbol{w}$, such that $d\boldsymbol{w} = \Omega_{\mathrm{L}} d\boldsymbol{U}$, we obtain

$$\frac{\partial \boldsymbol{w}}{\partial t} + \Lambda\frac{\partial \boldsymbol{w}}{\partial x} = 0, \tag{5}$$

or

$$\frac{\partial w_i}{\partial t} + \lambda_i\frac{\partial w_i}{\partial x} = 0, \quad i = 1, \ldots, 8, \tag{6}$$

where $\boldsymbol{w} = [w_1, w_2, \ldots, w_8]^{\mathrm{T}}$.

We implicitly assumed here that the x-axis is perpendicular to a chosen boundary of the computational regions, e.g., it can coincide with the radial direction on a spherical inner boundary placed into the lower corona.

It is clear from Equation (6) that the propagation of each w_i, which are called the characteristic variables, is described by an independent transport equation. Each of these equations are convection equations describing the propagation of w_i with the speed λ_i along the characteristic path $dx/dt = \lambda_i$.

Thus, physical boundary conditions should be specified only for characteristic variables that enter the computational region. For the entrance boundaries, this corresponds to $\lambda_i > 0$. For the system of ideal MHD equations, we have eight eigenvalues:

$$\lambda_{1,2} = u,\ \lambda_{3,4} = u \pm c_{\rm s},\ \lambda_{5,6} = u \pm c_{\rm A},\ \lambda_{7,8} = u \pm c_{\rm f}, \quad (7)$$

where $c_{\rm s}$, $c_{\rm A}$, and $c_{\rm s}$ are the slow magnetosonic, Alfvén, and fast magnetosonic speeds, respectively.

Thus the number of boundary conditions is not arbitrary and depends on the number of positive eigenvalues. Such boundary conditions are called physical. The rest of boundary conditions are mathematical. Clearly, only certain components of the vector of characteristic variables should be specified as physical. Unfortunately, there are no analytic expressions for w_i in MHD. In addition, one would prefer to specify measurable quantities as physical boundary conditions. For this to be possible, the time increments of such quantities should be uniquely expressible in terms of the time increments of physical w_i. A more detailed description can be found in Yalim et al. (2017). For example, if $u > c_{\rm f}$, all physical quantities should be specified at the inner spherical boundary. If $c_{\rm A} < u < c_{\rm f}$, only seven physical boundary conditions are possible, the remaining unknown variable should be found by solving the system of MHD equations.

Our model is designed to be driven by a variety of observational data, primarily by the *Solar Dynamics Observatory* (Pesnell et al. 2012)/Helioseismic and Magnetic Imager (Schou et al. 2012) (*SDO*/HMI) synoptic/synchronic vector magnetogram data (Liu et al. 2017). The horizontal velocity components are obtained by applying the differential affine velocity estimator for vector magnetograms (DAVE4VM; Schuck 2008; Liu et al. 2013) and the time–distance helioseismology methods (Zhao et al. 2012) to the HMI vector magnetogram data. In addition, our model can also be driven by line-of-sight (LOS) magnetogram data obtained by HMI, the *Solar and Heliospheric Observatory* (*SOHO*; Domingo et al. 1995)/Michelson Doppler Imager (Scherrer et al. 1995), National Solar Observatory/Global Oscillation Network Group (NSO), and Wilcox Solar Observatory. There is also a possibility of utilizing differential rotation (Komm et al. 1993a) and meridional flow (Komm et al. 1993b) formulae for horizontal velocity at high latitudes where the time–distance helioseismology method data do not exist.

We solve the set of ideal MHD equations in the heliocentric, inertial, or corotating frame of reference, using volumetric heating source terms to model solar wind acceleration by taking the 3D global magnetic field structure in the solar corona into account (Nakamizo et al. 2009; Feng et al. 2010). They are written in corotating frame with the Sun, in terms of conservative variables, in conservation-law form as follows:

$$\frac{\partial}{\partial t}\begin{pmatrix}\rho\\ \rho\boldsymbol{v}\\ \boldsymbol{B}\\ E\end{pmatrix} + \nabla\cdot\begin{pmatrix}\rho\boldsymbol{v}\\ \rho\boldsymbol{v}\boldsymbol{v} + \boldsymbol{I}\left(p + \frac{B^2}{8\pi}\right) - \frac{\boldsymbol{B}\boldsymbol{B}}{4\pi}\\ \boldsymbol{v}\boldsymbol{B} - \boldsymbol{B}\boldsymbol{v}\\ \left(E + p + \frac{B^2}{8\pi}\right)\boldsymbol{v} - \frac{\boldsymbol{B}}{4\pi}(\boldsymbol{v}\cdot\boldsymbol{B})\end{pmatrix} = \begin{pmatrix}0\\ \rho[\boldsymbol{g} + (\boldsymbol{\Omega}\times\boldsymbol{r})\times\boldsymbol{\Omega} + 2(\boldsymbol{v}\times\boldsymbol{\Omega})] + \boldsymbol{S}_M\\ 0\\ \rho\boldsymbol{v}\cdot[\boldsymbol{g} + (\boldsymbol{\Omega}\times\boldsymbol{r})\times\boldsymbol{\Omega}] + S_E\end{pmatrix}, \quad (8)$$

where $\rho, \boldsymbol{v}, \boldsymbol{B}$, p, E, and $\boldsymbol{g}$ are the density, velocity, magnetic field, thermal pressure, specific total energy of the plasma, and gravitational acceleration, respectively. The source terms in the momentum and energy conservation equations include the Coriolis and centrifugal forces, which are present only when the system is solved in a frame corotating with the Sun. Accordingly, $\boldsymbol{\Omega}$ and $\boldsymbol{r}$ correspond to the angular velocity of the Sun and position vector, respectively.

To model the solar wind acceleration, we introduce a volumetric heating source term, S_E, into the energy conservation equation, and the corresponding source term, $\boldsymbol{S}_M$, into the conservation of momentum equations (Nakamizo et al. 2009; Feng et al. 2010). They are given as follows:

$$S_E = \frac{Q_0}{f_s}\exp\left(-\frac{r}{L_Q}\right) + \nabla\left(\xi T^{2.5}\frac{\nabla T\cdot\boldsymbol{B}}{B^2}\right)\cdot\boldsymbol{B}, \quad (9)$$

where the first term is an ad hoc heating function and the second term is a thermal conduction term of the *Spitzer* type, and

$$\boldsymbol{S}_M = \frac{M_0}{f_s}\left(\frac{r}{R_\odot} - 1\right)\exp\left(-\frac{r}{L_M}\right), \quad (10)$$

where T is the plasma temperature, $L_{\rm M}$, $L_{\rm Q}$, M_0, and Q_0 are the model constants given as $L_{\rm M} = L_Q = 0.9\,R_\odot$, $M_0 = 2.65 \times 10^{-14}\,{\rm N\,m^{-3}}$, and $Q_0 = 1.65 \times 10^{-6}\,{\rm J\,m^{-3}\,s^{-1}}$. Additionally, f_s is the expansion factor by which a magnetic flux tube expands in solid angle between its footpoint location on the photosphere and the source surface which is typically at $R_{\rm SS} = 2.5\,R_\odot$ (Wang & Sheeley 1997):

$$f_s = \frac{B(R_\odot)}{B(R_{SS})}\left(\frac{R_\odot}{R_{SS}}\right)^2. \quad (11)$$

These source terms take the coronal magnetic field topology into account by incorporating the expansion factor.

The expansion factor is computed in every cell located between the inner boundary and the source surface according to the field-line tracing algorithm applied along the magnetic field lines presented in Cohen (2015). The expansion factor depends on the evolution of the coronal magnetic field with distance from the Sun in the background solar wind solution. After a CME is introduced into the background solar wind, the expansion factor remains unchanged. Otherwise, the force imbalance created by the flux rope inserted into background solar wind results in unphysical results. Besides, the quasi-steady background solar wind solution that interacts with the CME has already a well-established coronal magnetic field structure and the expansion factor associated with it. We will later demonstrate a good overall agreement of the CME speed between our simulation results and observational data and in this way justify our treatment of the expansion factor.

We calculate the initial solution for magnetic field with a potential field source surface (PFSS) model (Altschuler & Newkirk 1969; Schatten et al. 1969) using either a spherical harmonics approach (Hoeksema 1984; Wang & Sheeley 1992; Schrijver & DeRosa 2003) or a finite difference method by incorporating the solution provided by the Finite Difference Iterative Potential-field Solver code (Toth et al. 2011). For the rest of the plasma parameters, we compute the initial solution from Parker's isothermal solar wind model (Parker 1958).

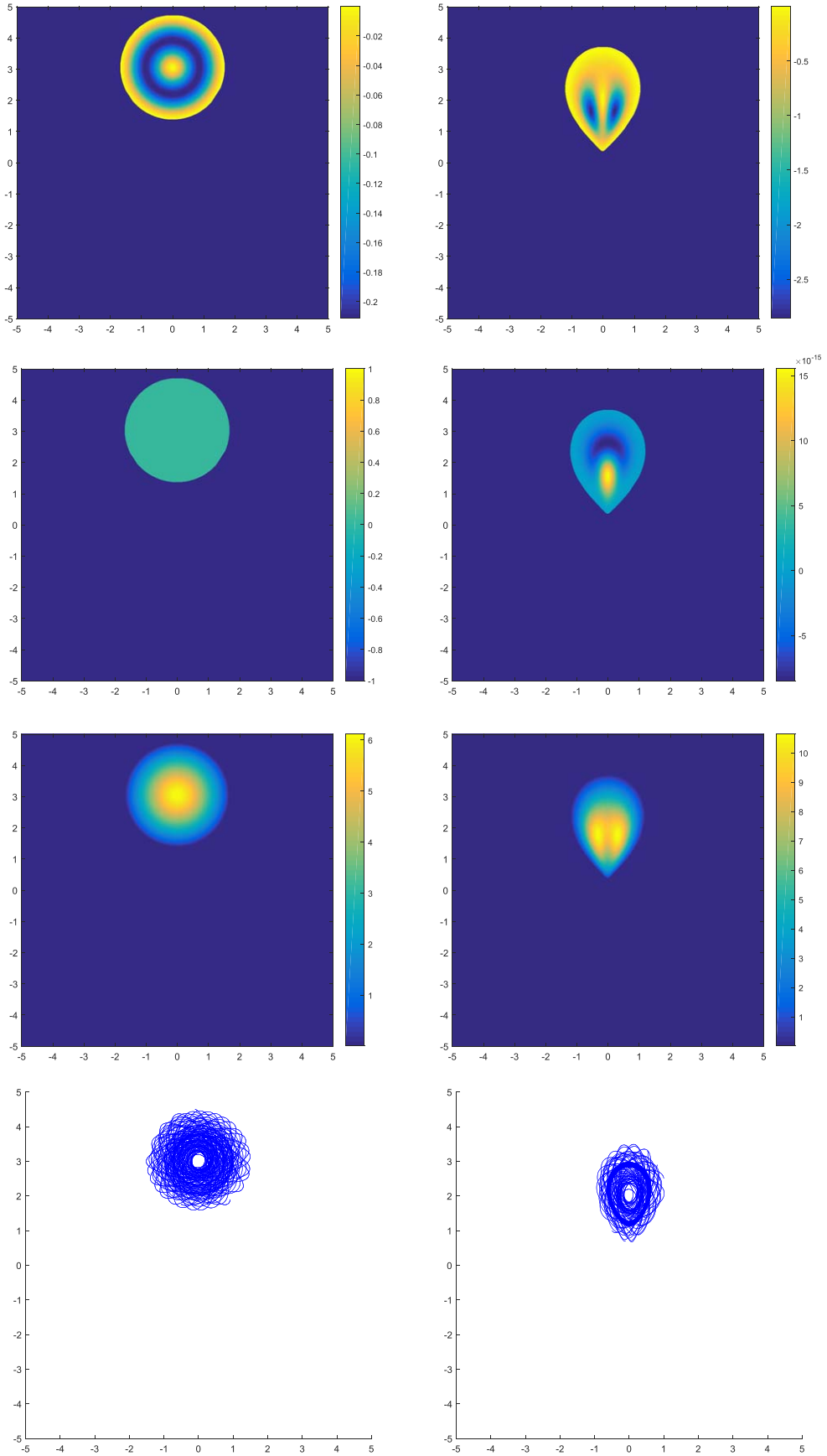

Figure 1. From top to bottom: pressure (dyne cm^{-2}), density (g cm^{-3}), magnetic field magnitude (G), and magnetic filed lines in unstretched (left) and stretched (right) GL torus. All horizontal and vertical axis are in $R_{\odot}$. We used $r_0 = 1.67$, $r_1 = 3.03$, $a = 1.01$, and $a_1 = 0.23$ in these figures. (0, 0) coordinate represents solar center.

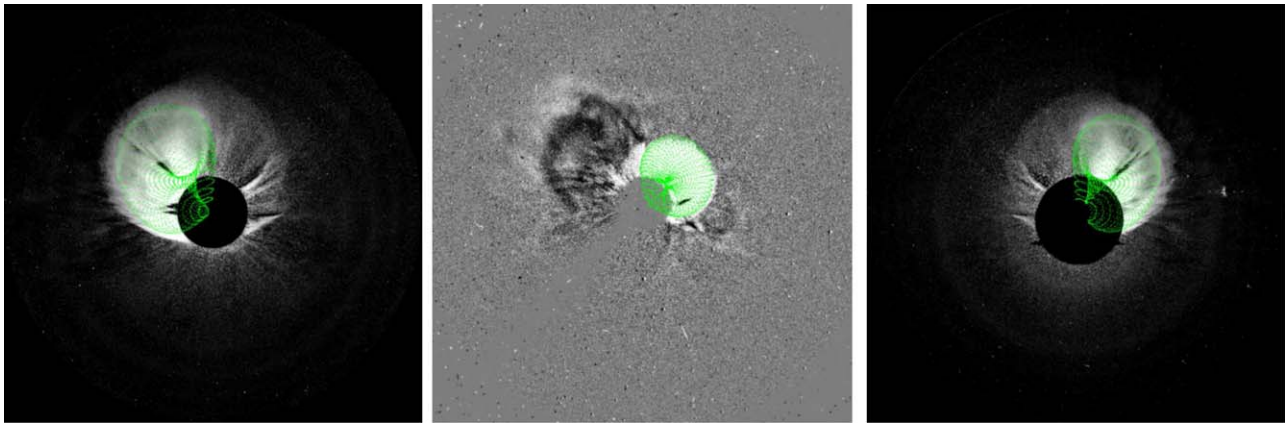

Figure 2. GCS fitting of a CME using three viewpoints (left and right panels): SECCHI/Cor2 onboard *STEREO A* and *B* respectively, and (middle panel) LASCO/C3 onboard *SOHO*.

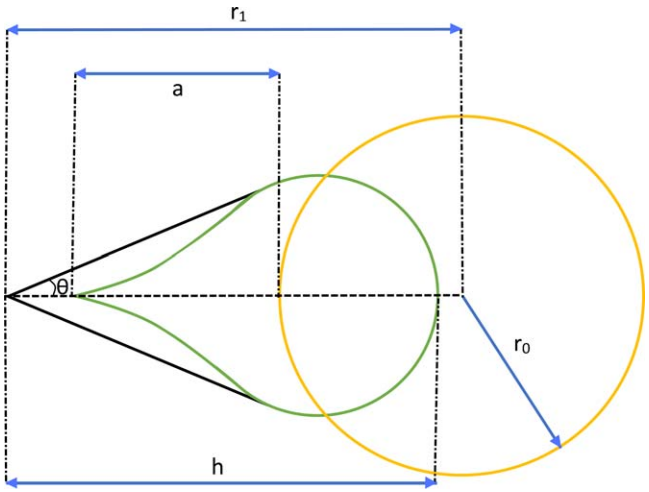

Figure 3. Diagram showing the GL sphere (yellow), its stretched tear drop shape (green), and GCS fit outline (black).

2.2. Gibson–Low Flux Rope Model

Solution to a GL flux rope is found by assuming balance of magnetic, pressure gradient and gravity forces. This can be written as $(\nabla \times \boldsymbol{B}) \times \boldsymbol{B} - \nabla p - \rho \boldsymbol{g} = 0$, where $\boldsymbol{B}$ is the magnetic field, p is the pressure, ρ is the density, and $\boldsymbol{g}$ is the gravitational acceleration. To define a GL flux rope, we also use the Gauss's law of magnetism, i.e., $\nabla \cdot \boldsymbol{B} = 0$. After deriving an analytical solution to $\boldsymbol{B}$ in the form of a spherical torus, a stretching transformation of $r \rightarrow r - a$ is used in spherical coordinates, where r is the radial coordinate and a is the stretching parameter. This results in a spherical torus of magnetic field lines being stretched into a tear drop shape. The analytical solution for a GL flux rope requires four parameters:

1. Flux rope radius (r_0): this is the radius of an initial GL spherical torus before stretching.
2. Flux rope height (r_1): this is the height of the center of the introduced spherical torus with respect to the center of the Sun before stretching.
3. Flux rope stretching parameter (a): this is the amount by which each part of the spherical torus is stretched toward the center of the Sun.
4. Flux rope field strength (a_1): this is a free parameter that controls the field strength in the flux rope being introduced. Plasma pressure inside the rope is proportional to a_1^2 due to the condition of pressure balance assumed in this solution.

Figure 1 shows pressure, density, magnetic field magnitude, and magnetic field lines in the plane containing the centroidal axis of a spherical torus before and after the stretching operation. Notice that density is introduced only after stretching, since no force is associated with it before stretching.

2.3. Data-constrained CME Model Using Graduated Cylindrical Shell Method

We utilize the Sun–Earth Connection Coronal and Heliospheric Investigation (SECCHI)/Cor1/Cor2 (Howard et al. 2008) coronagraph image data from *STEREO A* and *B* (Kaiser et al. 2008) and Large Angle Spectroscopic Coronagraph (LASCO)/C2/C3 (Brueckner et al. 1995) data from *SOHO* as observational data to constrain the GL flux rope parameters. We apply the GCS method to find the height, (h), direction and half angle, (θ), (from the central axis to the outer edge) of the CME as shown in Figures 2 and 3. GCS fitting is a visual fitting tool where three viewpoints of a CME from *STEREO A* and *B* and *SOHO* coronagraphs are used to fit the flux rope structure with conical legs and curved fronts over a CME. The GCS method was implemented in IDL using the *rtsccguicloud* program (Thernisien et al. 2006). The size parameters of a GL flux rope r_0, r_1, and a can be approximately related to the GCS size parameters according to the geometry shown in Figure 3.

We work under the assumption that $a = r_1/3$ and the front edge of tear drop shape roughly matches the front end of GCS shape. In fact, by comparing the curved fronts of the tear drop and GCS shapes, we find that if we vary r_0 from 0.4 to 2 $R_\odot$ and r_1 from 1.5 to 5 $R_\odot$, the maximum distance between the two shapes is always less than 5% of r_1. Therefore, the two shapes coincide very well. Therefore,

$$h + a = r_1 + r_0, \tag{12}$$

$$h - r_0 = \frac{2}{3} r_1, \tag{13}$$

$$h - r_1 \sin\theta = \frac{2}{3} r_1. \tag{14}$$

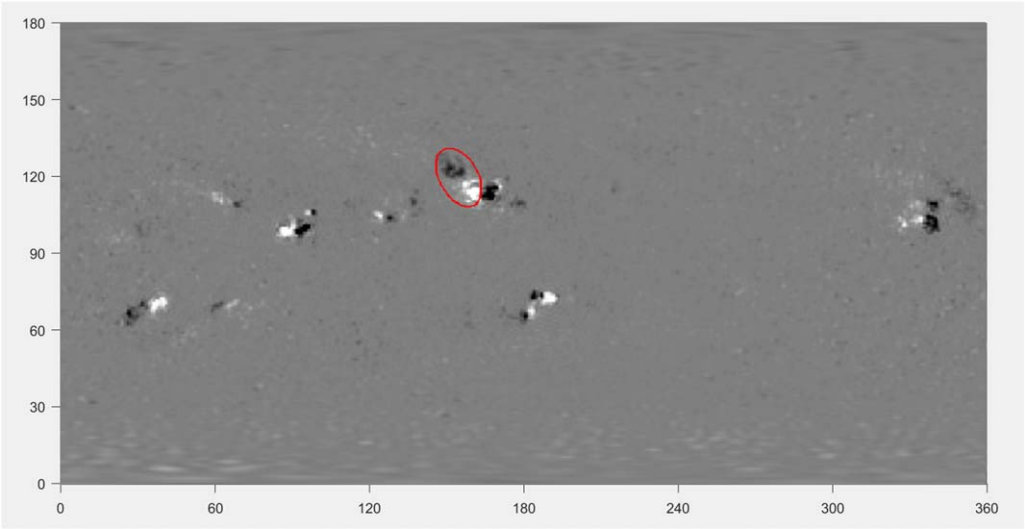

Figure 4. HMI LOS magnetogram obtained on 2011 March 7 at 06:00 UT with the source active region from which the CME erupted is indicated in red.

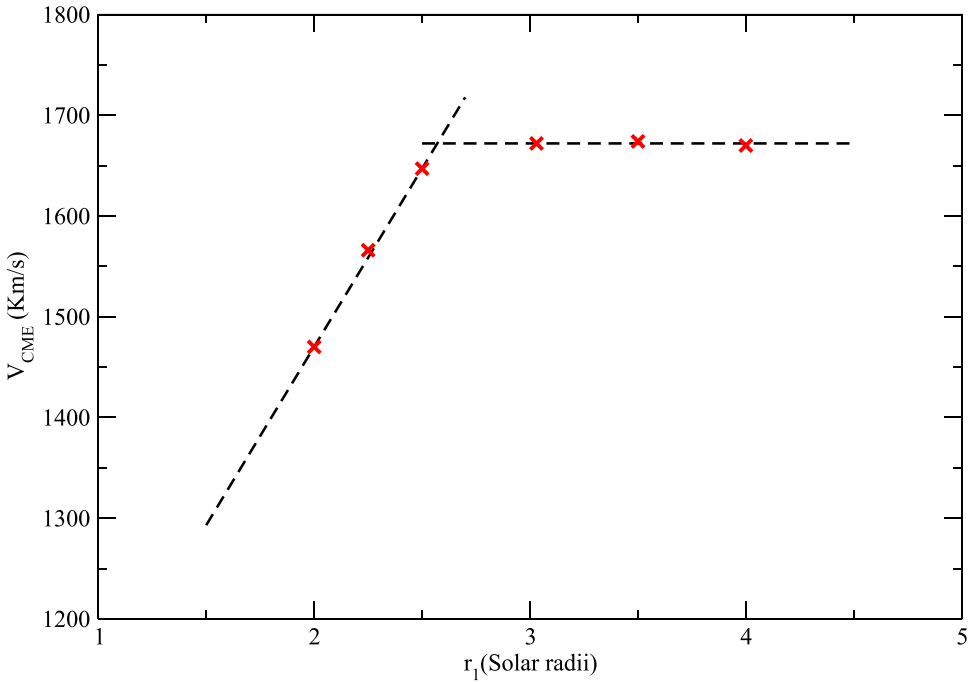

Figure 5. Variation of CME speed with r_1.

This gives us

$$r_1 = \frac{h}{2/3 + \sin\theta}; \quad a = \frac{h}{2 + 3\sin\theta}; \quad r_0 = \frac{h\sin\theta}{2/3 + \sin\theta}. \tag{15}$$

We notice that this approach constrains us to using the relation $r_0 = r_1 \sin\theta$. However, r_1 and r_0 are independent parameters in GL analytical formulae. Therefore, the dependence of r_0 on r_1 is only due to the observational limitations.

The remaining GL parameter (i.e., magnetic field strength, a_1) cannot be determined from observations directly. Therefore, we perform a parametric study to find an expression for a_1 in terms of r_0, r_1, the average simulated solar wind pressure above the erupting region, $P_{\rm avg}$, and speed of a CME, $V_{\rm CME}$. The latter can be found by applying linear fitting to the height versus time data from the GCS method. To calculate $P_{\rm avg}$, we find average pressure in simulated solar wind in $\pm 30^\circ$ latitude and longitude from inner boundary to $10\,R_\odot$.

2.3.1. Parametric Study

We follow the method used by Jin et al. (2017a) to perform the parametric study. Here, we check the effect of changes in the input GL flux rope parameters on the CME speed. In contrast to Jin et al. (2017a), we additionally allow variations in r_1. There is also a possibility of using GCS size parameters for parametric study but, as we will show below, using GL size parameters gives results in form of simple linear functions. To

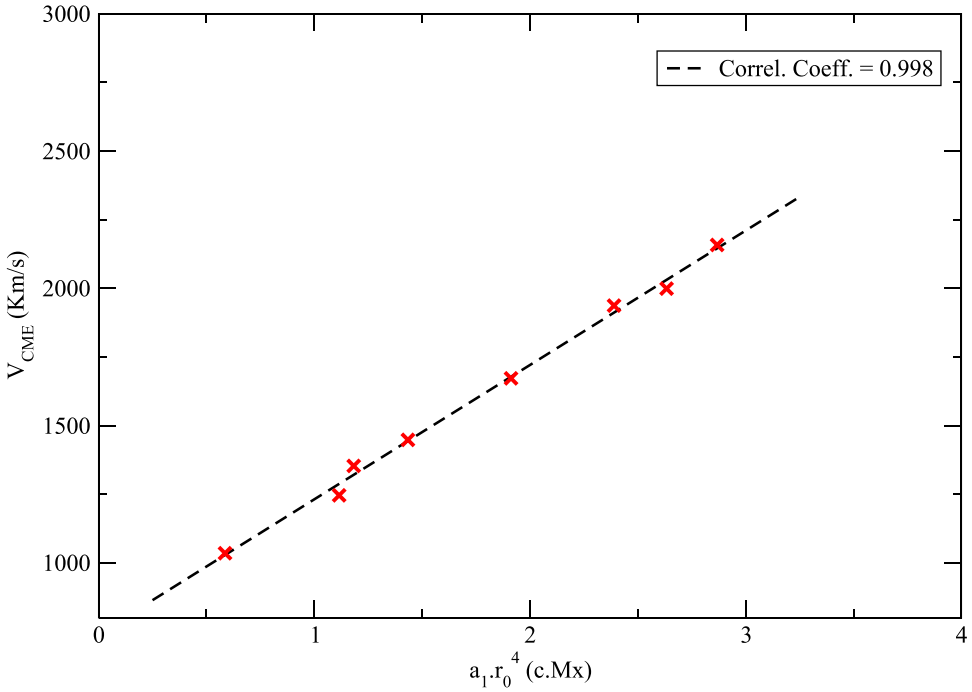

Figure 6. Variation of CME speed with poloidal flux ($\phi \propto a_1 r_0^4$).

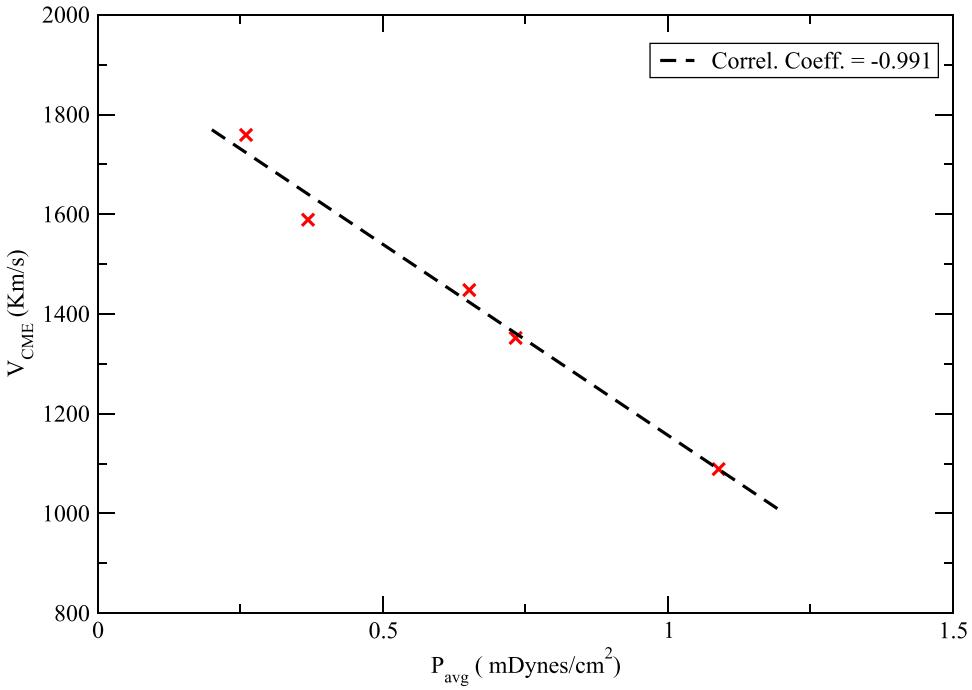

Figure 7. Variation of CME speed with $P_{\rm avg}$.

Table 1
Parameters Used in the Expression of a_1

r_1	c_1	c_2	c_3	c_4	c_5	c_6
<2.6	3.849	5.831	−6.018	15.112	2.783	6.009
$\geqslant 2.6$	13.018	19.721	−20.354	51.112		

perform the parametric study, we need to select a magnetogram with multiple active regions. At least one of the active regions should have ejected a CME in such a direction that the CME parameters can be easily determined by the GCS method. In this study, we select the HMI LOS magnetogram from 2011 March 7 06:00 UT, in which one of the active regions numbered AR11164 produced a fast CME that occurred on 2011 March 7 at 20:00 UT (see Figure 4). We determine the size parameters of the GL flux rope corresponding to this CME as $r_0 = 1.68$, $r_1 = 3.03$ and $a = 1.01$ using the GCS method.

We perform our parametric study in three steps. First, a GL flux rope with $r_0 = 1.68$, $a_1 = 0.24$, and varying r_1 is kept on the source active region (AR11164) and the simulated CME speed is calculated (see Figure 5). Then, we fix $r_1 = 3.03$ and

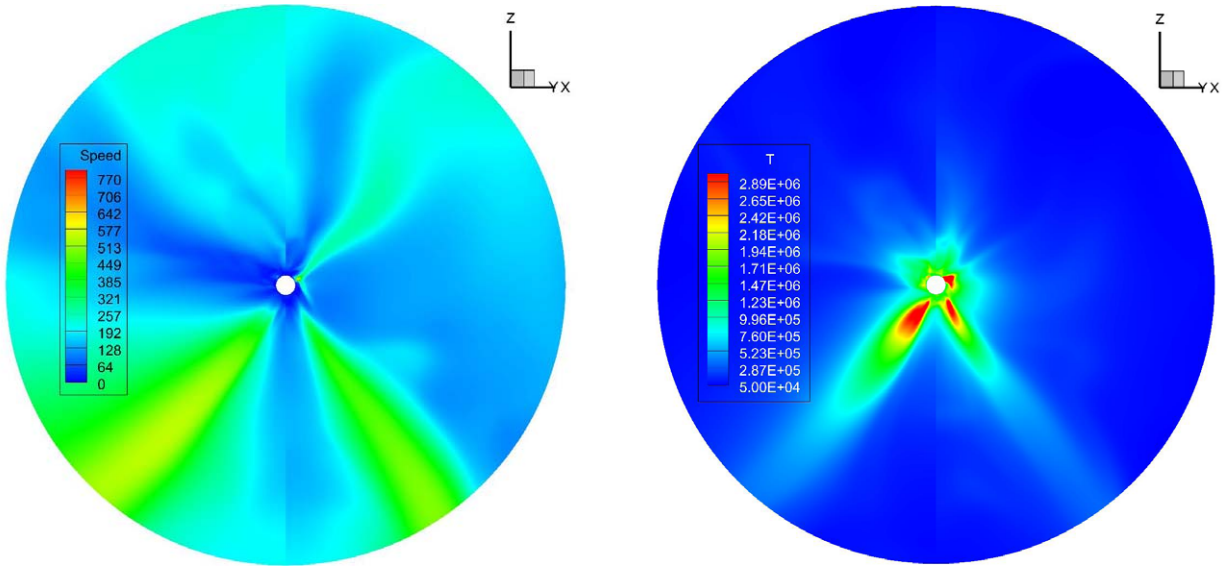

Figure 8. Solar wind background simulated using HMI LOS magnetogram of 2011 March 7 06:00 UT: (left) speed contours (km s^{-1}); (right) temperature contours (K). The background is shown in the plane in which flux rope is introduced.

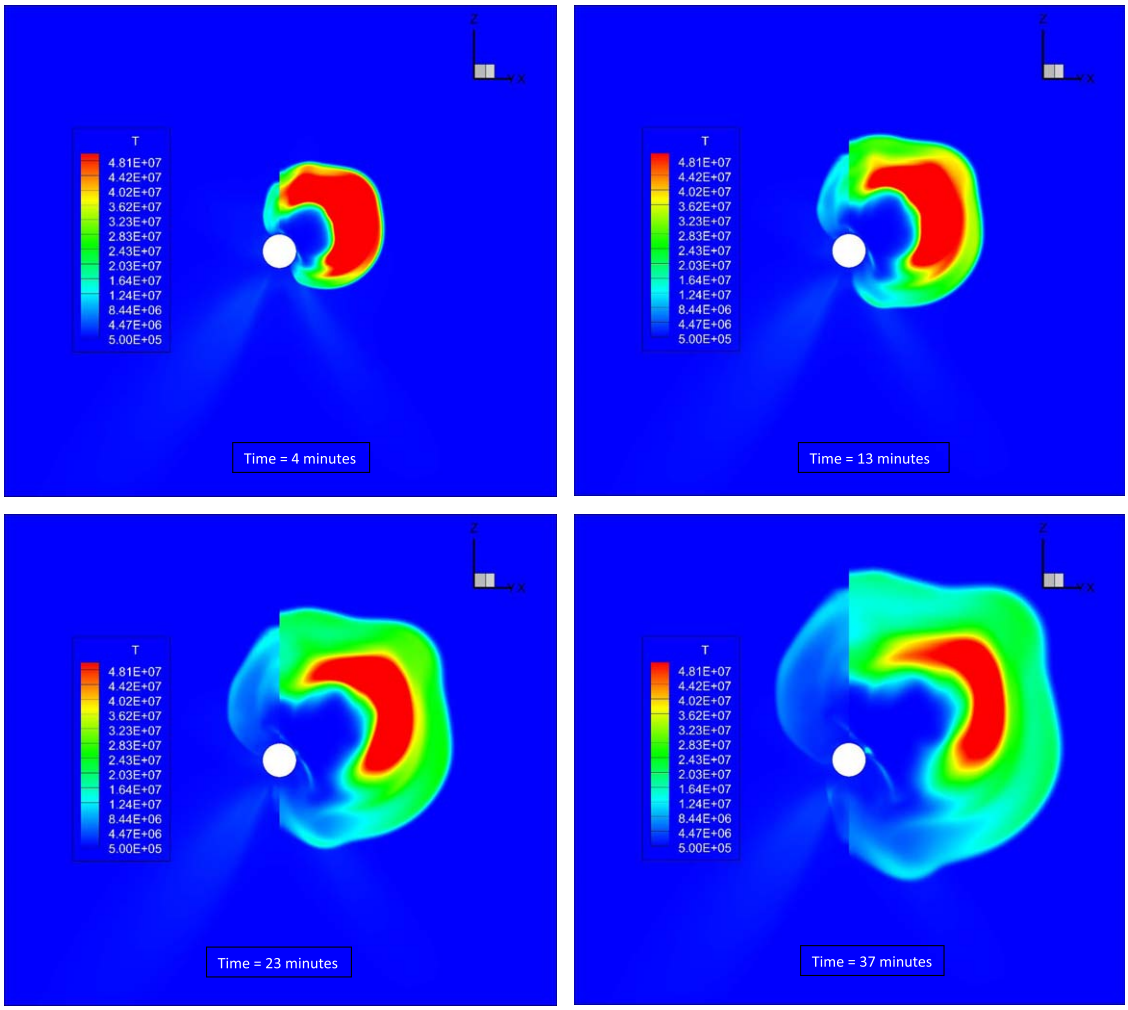

Figure 9. Time evolution of the CME shown using temperature contours.

the poloidal flux, ϕ, is varied by changing r_0 and a_1, while still keeping the flux rope at the same source active region (see Figure 6). Poloidal flux of a GL flux rope can be determined by integrating the magnitude of poloidal magnetic field component over the surface perpendicular to the polar axis of GL spherical torus. It can be shown that $\phi \propto a_1 r_0^4$ (Jin et al. 2017a). Finally,

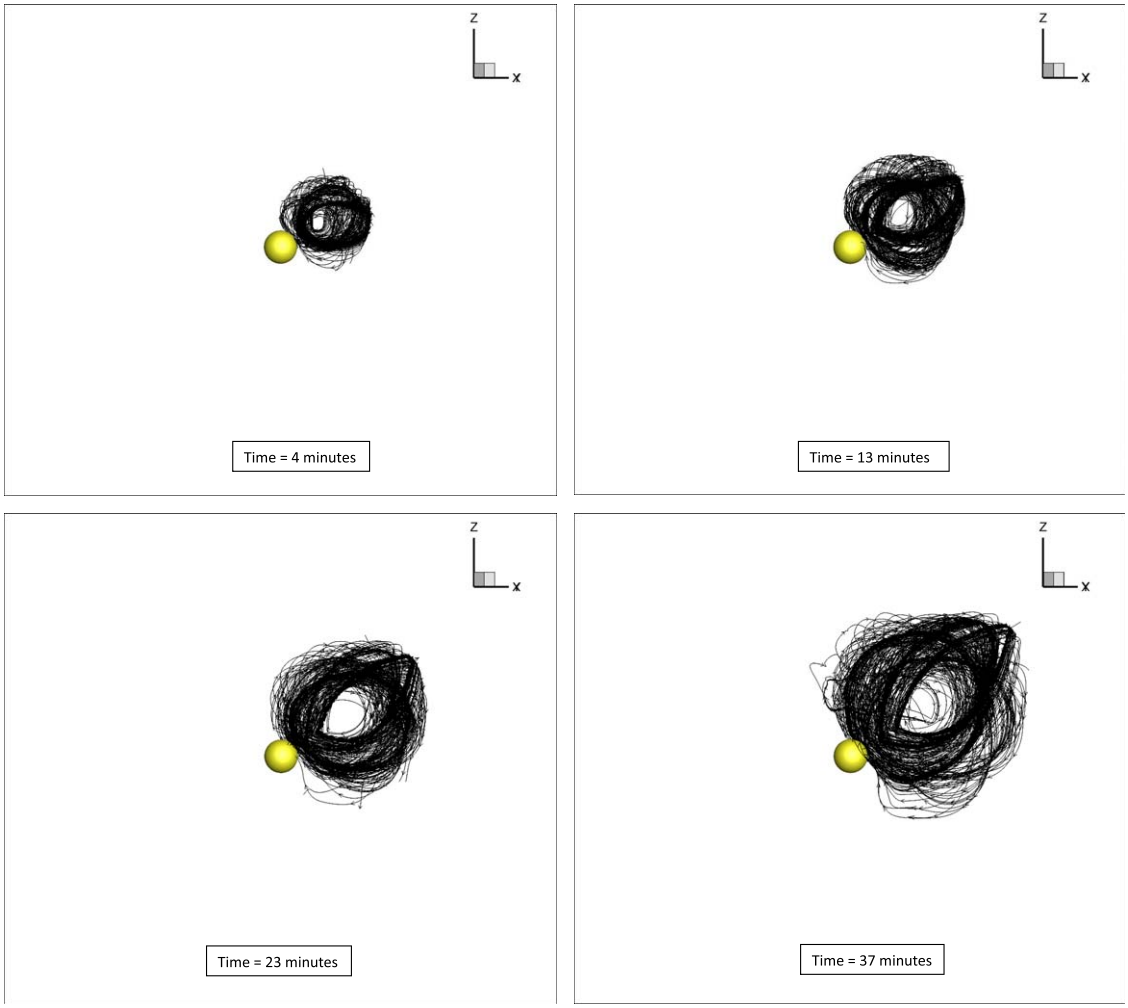

Figure 10. Time evolution of the CME shown using magnetic field lines of flux rope.

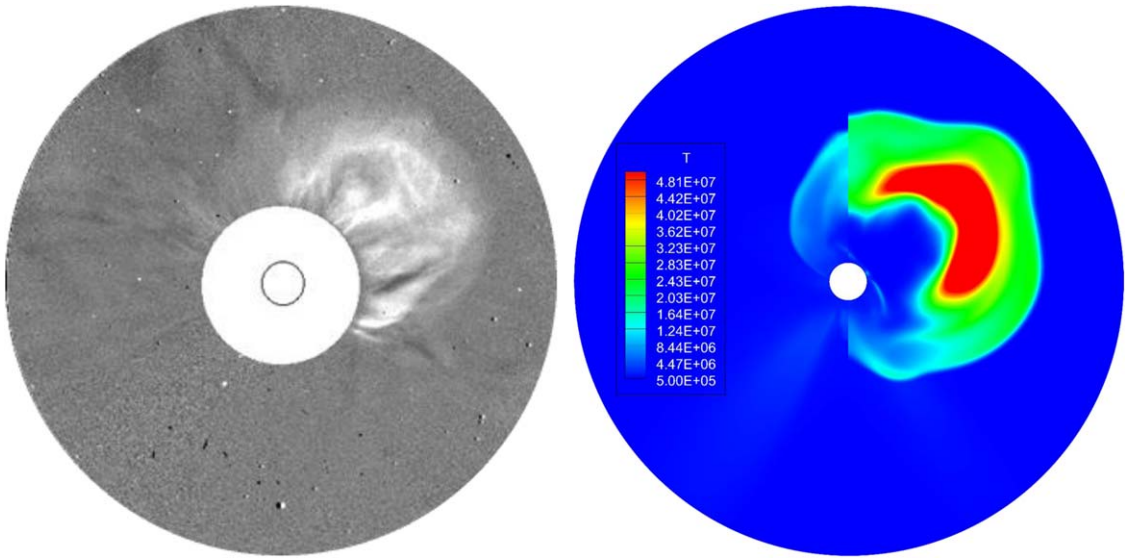

Figure 11. Comparison of CME shapes: (left panel) LASCO/C3 coronagraph difference image; (right panel) temperature contours obtained from the simulation.

we place the same flux rope with parameters $r_0 = 1.68$, $a_1 = 0.18$ and $r_1 = 3.03$ over different active regions with different $P_{\rm avg}$'s and determine the variation in the simulated CME speed (see Figure 7).

We combine all these steps to derive an expression for a_1 as follows:

$$V_{\rm CME} = f_1(\phi) \cdot f_2(P_{\rm avg}) \cdot f_3(r_1). \quad (16)$$

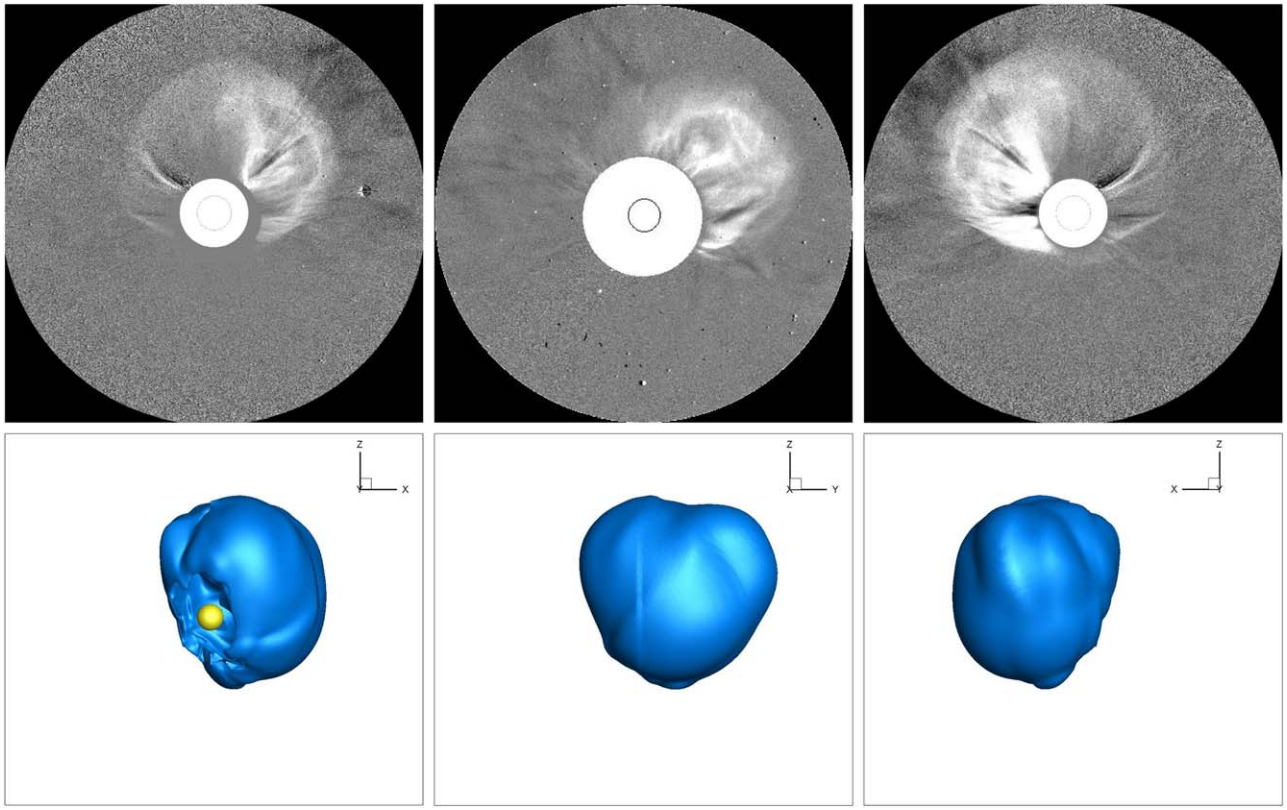

Figure 12. Comparison of CME shapes from points of view of *SOHO*, *STEREO A* and *B*: (upper row) from left to right: Cor2 (*STEREO B*), LASCO/C3, Cor2 (*STEREO A*); (lower row) temperature Iso-surface indicating the CME shape in the same orientation as the corresponding image in the upper row and having same scales.

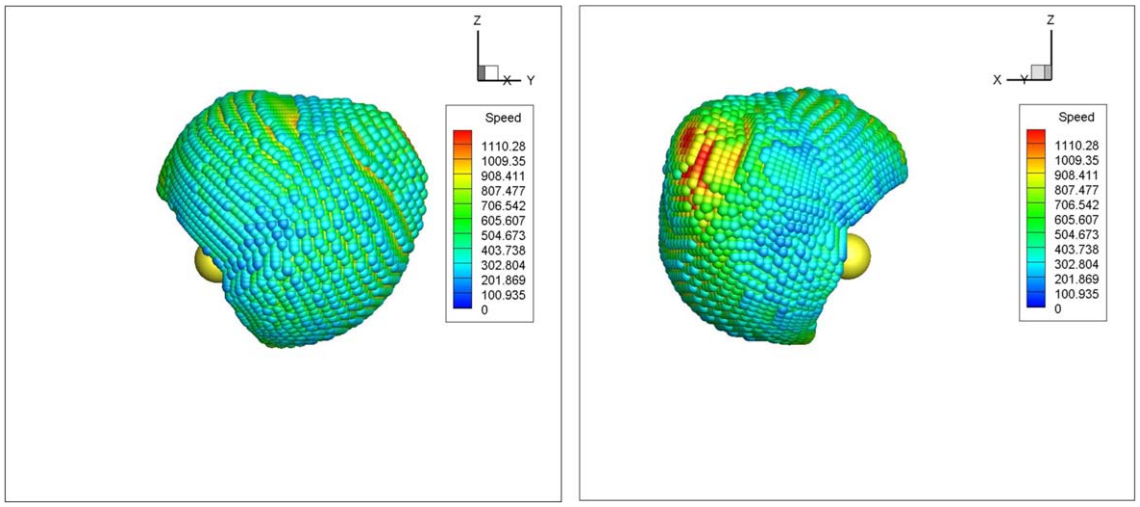

Figure 13. Shock surface in front of the simulated CME from two different viewpoints at 23 minutes after eruption.

The parametric study shows that f_1 and f_2 are linear functions whereas f_3 is linear for $r_1 < 2.6$ and constant for $r_1 \geqslant 2.6$. There is an explanation for the latter behavior. When we keep the stretched GL flux rope closer to the Sun, most of its lower part resides under solar surface and full energy of the GL flux rope is therefore not injected into the background solar wind. We also note that Jin et al. (2017a) use active region magnetic field strength B_r instead of $P_{\rm avg}$ to differentiate between different locations where flux rope is kept initially. We find that $P_{\rm avg}$ shows much better correlation with $V_{\rm CME}$ than B_r.

Keeping the above in mind, we can write out

$$V_{\rm CME} = \begin{cases} (c_1 a_1 r_0^4 + c_2) \cdot (c_3 P_{\rm avg} + c_4) \cdot (c_5 r_1 + c_6) & r_1 < 2.6 \\ (c_1 a_1 r_0^4 + c_2) \cdot (c_3 P_{\rm avg} + c_4) & r_1 \geqslant 2.6. \end{cases} \quad (17)$$

Now, we use nonlinear multi-variable regression on all the CME runs in the parametric study to find the fitting constants. The results are given in Table 1. Finally, the expression for a_1

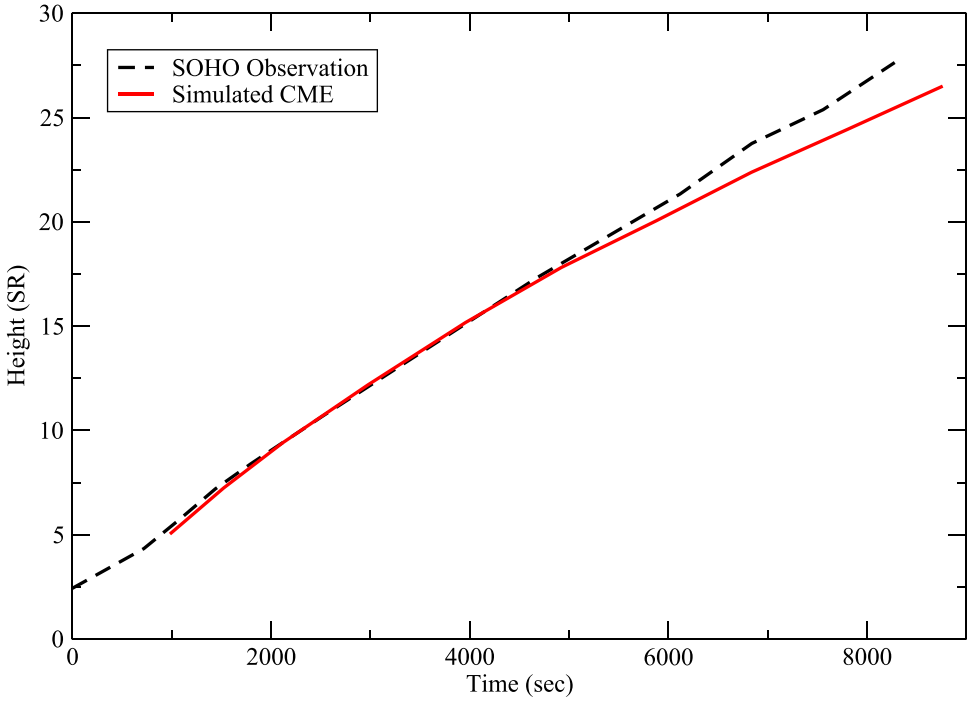

Figure 14. Comparison of height vs. time graphs between LASCO/C3 observations and simulation results.

can be written as follows:

$$a_1 = \begin{cases} \dfrac{1}{c_1 r_0^4} \cdot \left(\dfrac{V_{\rm CME}}{(c_3 P_{\rm avg} + c_4) \cdot (c_5 r_1 + c_6)} - c_2 \right) & r_1 < 2.6 \\ \dfrac{1}{c_1 r_0^4} \cdot \left(\dfrac{V_{\rm CME}}{(c_3 P_{\rm avg} + c_4)} - c_2 \right) & r_1 \geqslant 2.6. \end{cases} \quad (18)$$

3. Simulation Results

In this section, we show the results related to our simulation of the eruption of the fast CME that occurred on 2011 March 7 at 20:00 UT. The background solar wind solution is obtained by relaxing the initial PFSS magnetic field distribution to steady state using our data-driven MHD global solar corona model. We computed the initial conditions for magnetic field corresponding to the simulation made to obtain the background solar wind solution from the PFSS model by using the spherical harmonics coefficients corresponding to the HMI LOS magnetogram on 2011 March 7 obtained from the *pfss_viewer* program on IDL SolarSoft. The initial conditions for the remaining hydrodynamic plasma variables were obtained from Parker's isothermal solar wind model. We used the Vikentios Damodos Telescope (TVD), finite volume Rusanov scheme (Kulikovskii et al. 2001) to compute the numerical fluxes and the forward Euler scheme for time integration. To satisfy the solenoidal constraint, we applied Powell's source term method (Powell et al. 1999). Our computational domain size is $1.03\,R_\odot \leqslant r \leqslant 30\,R_\odot$, $0 \leqslant \phi \leqslant 2\pi$, $0 \leqslant \theta \leqslant \pi$ and grid size is $180 \times 240 \times 120$ in r, ϕ, and θ directions, respectively. We perform all simulations in the frame corotating with the Sun. MS-FLUKSS provides us with parallel implementation of the numerical methods. At the inner boundary of the computational domain which is located at the lower corona, we applied the radial magnetic field derived from the HMI LOS magnetogram data and the differential rotation (Komm et al. 1993a) and meridional flow (Komm et al. 1993b) formulae for the horizontal velocity components at the ghost cell centers. We kept density and temperature constant as $n = 1.5 \times 10^8\,{\rm cm}^{-3}$ and $T = 1.3 \times 10^6$ K, respectively. The radial velocity component is imposed to be zero at the boundary surface. The transverse magnetic field components are extrapolated from the domain into the ghost cells. At the outer boundary of the domain, which is located beyond the critical point, the plasma flow is superfast magnetosonic, so no boundary conditions are required. The computational domain, grid size, numerical methods, and boundary conditions are the same for all the runs performed. Figure 8 shows the background through which we propagate the CME.

We use $V_{\rm CME} = 2125$ km s^{-1} for the fast CME that occurred on 2011 March 7 as given by the *SOHO* CME catalog (Gopalswamy et al. 2009). We also found $r_0 = 1.68$, $r_1 = 3.03$ and $a = 1.01$ from the GCS method for this CME. The pressure $P_{\rm avg}$ is found to be 0.652 mdyne cm^{-2}. Using these values and the calculated coefficients in Table 1 in Equation (18), we find $a_1 = 0.35$. Running our simulation with this value of a_1 and the GL size parameters, we find the simulated speed to be 2140 km s^{-1}, which is very close to the actual speed. Figure 9 shows the time evolution of simulated CME using temperature contours, whereas Figure 10 shows the same time evolution using magnetic flux rope structure of the CME. Figures 11 and 12 shows the comparison of the simulated CME shape with the coronagraph observations. The shape of CME is approximated by an iso-surface of the temperature.

Figure 13 shows the shock surface propagating in front of the CME. Its surface is colored according to speed values. The shock surface is found by locating the jump in entropy along radial direction with a resolution of 2° in latitude and longitude. Shock properties derived from our simulation can be used to model SEP events. Hu et al. (2018) have recently used CME driven shocks to model SEP acceleration using their improved

Particle Acceleration and Transport in the Heliosphere (iPATH) model. However, they note that more realistic treatment of CMEs in simulations, like using flux rope models, can enhance the accuracy of their results and better understand the solar energetic particles (SEP) events.

Finally, Figure 14 shows the agreement between the height versus time graphs obtained from the LASCO/C3 observations and the simulation results.

4. Conclusions

In this paper, we presented a data-constrained CME model, which is based on the GL flux rope approach and uses the GCS method. Our CME model is complementary to the model described in Jin et al. (2017b), and has certain advantages over it. We determine the GL flux rope size parameters more accurately because of the application of the GCS method to *SOHO*/LASCO/C2/C3 and *STEREO A* and *B*/SECCHI/Cor1/Cor2 coronagraph image data. Thus, we do not impose excessive energy in the initial flux rope configuration, thereby avoiding excessive heating and acceleration of the flux rope. Determining the size parameters from the GCS method results in a realistic initial flux rope size in agreement with the observations, which leads to correct CME speed and acceleration.

These results do not imply that our CME model is better than models involving energy buildup before eruption (e.g., Amari et al. 2014; Török et al. 2018). However, due to its simplicity, our approach is less time consuming. Besides, it has obvious advantages over the "blob" and "cone" models because of a more realistic treatment of magnetic field.

Now, when it is demonstrated that our data-constrained CME generation model works in the solar corona, we will propagate the same CME through the inner heliosphere and compare our simulation results with the near-Earth spacecraft data at 1 au. We also plan to investigate CME–CME interactions in the future following a simulation approach.

The authors acknowledge the support from the NASA project NNX14AF41G and NSF SHINE grant AGS-1358386. This work is also supported by the Parker Solar Observatory contract with the Smithsonian Astrophysical Observatory through subcontract SV4-84017. We also acknowledge NSF PRAC award ACI-1144120 and related computer resources from the Blue Waters sustained-petascale computing project. Supercomputer allocations were also provided on SGI Pleiades by NASA High-End Computing Program award SMD-16-7570 and on Stampede2 by NSF XSEDE project MCA07S033.

This work utilizes data from *SOHO* which is a project of international cooperation between ESA and NASA. The HMI data have been used courtesy of NASA/*SDO* and HMI science teams. The *STEREO*/SECCHI data used here were produced by an international consortium of the Naval Research Laboratory (USA); Lockheed Martin Solar and Astrophysics Lab (USA); NASA Goddard Space Flight Center (USA); Rutherford Appleton Laboratory (UK); University of Birmingham (UK); Max-Planck-Institut for Solar System Research (Germany); Centre Spatiale de Liège (Belgium); Institut d'Optique Théorique et Appliquée (France); and Institut d'Astrophysique Spatiale (France). This work uses *SOHO* CME catalog, which is generated and maintained at the CDAW Data Center by NASA and The Catholic University of America in cooperation with the Naval Research Laboratory.

ORCID iDs

T. Singh https://orcid.org/0000-0002-0213-6038
M. S. Yalim https://orcid.org/0000-0002-8496-0353
N. V. Pogorelov https://orcid.org/0000-0002-6409-2392

References

Adhikari, L., Zank, G. P., Bruno, R., et al. 2015, ApJ, 805, 63
Altschuler, M. D., & Newkirk, G. 1969, SoPh, 9, 131
Amari, T., Aly, J.-J., Luciani, J.-F., et al. 2011, ApJL, 742, L27
Amari, T., Canou, A., & Aly, J.-J. 2014, Natur, 514, 465
Antiochos, S. K., DeVore, C. R., & Klimchuk, J. A. 1999, ApJ, 510, 485
Aulanier, G. 2014, in Proc. IAU Symp. 300, ed. B. Schmieder, J.-M. Malherbe, & S. T. Wu (Cambridge: Cambridge Univ. Press), 184
Aulanier, G., Torok, T., Demoulin, P., et al. 2010, ApJ, 708, 314
Borovikov, D., Sokolov, I. V., Manchester, W. B., et al. 2017, JGR, 122, 7979
Borovikov, S. N., Heerikhuisen, J., & Pogorelov, N. V. 2013, in ASP Conf. Ser. 474, ASTRONUM 2012 Numerical Modeling of Space Plasma Flows, ed. N. V. Pogorelov, E. Audit, & G. P. Zank (San Francisco, CA: ASP), 219
Borovikov, S. N., Kryukov, I. A., & Pogorelov, N. V. 2009, in ASP Conf. Ser. 406, ASTRONUM 2008 Numerical Modeling of Space Plasma Flows, ed. N. V. Pogorelov et al. (San Francisco, CA: ASP), 127
Brueckner, G. E., Delaboudiniere, J.-P., Howard, R. A., et al. 1998, GeoRL, 25, 3019
Brueckner, G. E., Howard, R. A., Koomen, M. J., et al. 1995, SoPh, 162, 357
Chane, E., Jacobs, C., van der Holst, B., et al. 2005, A&A, 432, 331
Chen, P. F. 2011, LRSP, 8, 1
Cheung, M. C. M., Pontieu, B. D., Tarbell, T. D., et al. 2015, ApJ, 801, 83
Cohen, O. 2015, SoPh, 290, 2245
Colella, P., Bell, J., Keen, N., et al. 2007, J. Phys. Conf. Ser., 78, 012013
Detman, T. R., Intriligator, D. S., Dryer, M., et al. 2011, JGR, 116, 3105
Domingo, V., Fleck, B., & Poland, A. I. 1995, SoPh, 162, 1
Fan, Y., & Gibson, S. E. 2007, ApJ, 668, 1232
Feng, X., Ma, X., & Xiang, C. 2015, JGR, 120, 10159
Feng, X., Yang, L., Xiang, C., et al. 2010, ApJ, 723, 300
Feng, X., Zhang, S., Xiang, C., et al. 2011, ApJ, 734, 50
Fisher, G. H., Abbett, W. P., Bercik, D. J., et al. 2015, SpWea, 13, 369
Forbes, T. G., Linker, J. A., Chen, J., et al. 2006, SSRv, 123, 251
Forbes, T. G., & Priest, E. R. 1995, ApJ, 446, 377
Gamayunov, K. V., Zhang, M., Pogorelov, N. V., et al. 2012, ApJ, 757, 74
Gibson, S. E., & Low, B. C. 1998, ApJ, 493, 460
Gopalswamy, N., Lara, A., Manoharan, P. K., et al. 2005, AdSpR, 36, 2289
Gopalswamy, N., Yashiro, S., Michalek, G., et al. 2009, EM&P, 104, 295
Hayashi, K. 2013, JGR, 118, 6889
Hoeksema, J. T. 1984, PhD thesis, Stanford Univ.
Howard, R. A., Moses, J. D., Vourlidas, A., et al. 2008, SSRv, 136, 67
Hu, J., Li, G., & Fu, S. 2018, ApJL, 854, L19
Hu, Y. Q. 2001, SoPh, 200, 115
Intriligator, D. S., Detman, T., Gloecker, C., et al. 2012, JGR, 117, A06104
Jacobs, C., Poedts, S., & van der Holst, B. 2006, A&A, 450, 793
Jiang, C., Wu, S. T., Feng, X., et al. 2016, NatCo, 7, 11522
Jin, M., Manchester, W. B., van der Holst, B., et al. 2017a, ApJ, 834, 172
Jin, M., Manchester, W. B., van der Holst, B., et al. 2017b, ApJ, 834, 173
Jin, M., Schrijver, C. J., Cheung, M. C. M., et al. 2016, ApJ, 820, 16
Kaiser, M. L., Kucera, T. A., Davila, J. M., et al. 2008, SSRv, 136, 5
Kataoka, R., Ebisuzaki, K., Kusano, K., et al. 2009, JGR, 114, A10102
Kliem, B., & Torok, T. 2006, PhRvL, 96, 255002
Komm, R. W., Howard, R. F., & Harvey, J. W. 1993a, SoPh, 143, 19
Komm, R. W., Howard, R. F., & Harvey, J. W. 1993b, SoPh, 147, 207
Kryukov, I. A., Pogorelov, N. V., Zank, G. P., et al. 2012, in AIP Conf. Ser. 1436, Proc. 10th Annual Int. Astrophysics Conf., ed. J. Heerikhuisen et al. (Melville, NY: AIP), 48
Kulikovskii, A. G., Pogorelov, N. V., & Semenov, A. Y. 2001, in Hyperbolic Problems: Theory, Numerics, and Applications, ed. R. Jeltsch & M. Fey (Basel: Springer), 589
Leake, J. E., Linton, M. G., & Antiochos, S. K. 2014, ApJ, 787, 46
Lee, E., Lukin, V. S., & Linton, M. G. 2014, A&A, 569, A94
Lin, J., & Forbes, T. G. 2000, JGR, 105, 2375
Linker, J. A., Caplan, R. M., Downs, C., et al. 2016, J. Phys. Conf. Ser., 719, 012012
Linker, J. A., & Mikic, Z. 1995, ApJL, 438, L45
Lionello, R., Linker, J. A., & Mikic, Z. 2009, ApJ, 690, 902
Lionello, R., Torok, T., Titov, V. S., et al. 2016, ApJL, 831, L2
Liu, Y., Hoeksema, J. T., Sun, X., et al. 2017, SoPh, 292, 29

Liu, Y., Zhao, J., & Schuck, P. W. 2013, SoPh, 287, 279
Lockwood, M., Owens, M. J., Barnard, L. A., et al. 2016, SpWea, 14, 406
Lugaz, N., Manchester, W. B., & Toth, G. 2007, ApJ, 659, 788
Lugaz, N., Manchester, W. B., IV, & Gombosi, T. I. 2005, ApJ, 634, 651
Lugaz, N., & Roussev, I. I. 2011, JASTP, 73, 1187
Lugaz, N., Temmer, M., Wang, Y., et al. 2017, SoPh, 292, 64
Manchester, W. B., Gombosi, T. I., Roussev, I., et al. 2004a, JGR, 109, 2107
Manchester, W. B., Gombosi, T. I., Roussev, I., et al. 2004b, JGR, 109, 1102
Manchester, W. B., Ridley, A. J., Gombosi, T. I., et al. 2006, AdSpR, 38, 253
Manchester, W. B., IV, Kozyra, J. U., Lepri, S. T., et al. 2014a, JGR, 119, 5449
Manchester, W. B., IV, van der Holst, B., & Lavraud, B. 2014b, PPCF, 56, 064006
Manoharan, P. K., Gopalswamy, N., Yashiro, S., et al. 2004, JGR, 109, A06109
Merkin, V. G., Lionello, R., Lyon, J. G., et al. 2016, ApJ, 831, 23
Mikic, Z., & Linker, J. A. 1994, ApJ, 430, 898
Moon, Y.-J., Dryer, M., Smith, Z., et al. 2002, GeoRL, 29, 1390
Moore, R. L., Sterling, A. C., Hudson, H. S., et al. 2001, ApJ, 552, 833
Nakamizo, A., Tanaka, T., Kubo, Y., et al. 2009, JGR, 114, A07109
Odstrcil, D., & Pizzo, V. J. 1999, JGR, 104, 483
Odstrcil, D., & Pizzo, V. J. 2009, SoPh, 259, 297
Oran, R., Landi, E., van der Holst, B., et al. 2015, ApJ, 806, 55
Parker, E. N. 1958, ApJ, 128, 664
Pesnell, W. D., Thompson, B. J., & Chamberlin, P. C. 2012, SoPh, 275, 3
Poedts, S., & Pomoell, J. 2017, in Proc. EGU General Assembly Conf. Abstracts, 19, 7396
Pogorelov, N. V., Borovikov, S. N., Bedford, M. C., et al. 2013, in ASP Conf. Ser. 474, ASTRONUM 2012 Numerical Modeling of Space Plasma Flows, ed. N. V. Pogorelov, E. Audit, & G. P. Zank (San Francisco, CA: ASP), 165
Pogorelov, N. V., Borovikov, S. N., Florinski, V., et al. 2009, in ASP Conf. Ser. 406, ASTRONUM 2008 Numerical Modeling of Space Plasma Flows, ed. N. V. Pogorelov et al. (San Francisco, CA: ASP), 149
Pogorelov, N. V., Borovikov, S. N., Heerikhuisen, J., et al. 2014, in XSEDE'14 Proc. 2014 Annual Conf. on Extreme Science and Engineering Discovery Environment (New York: ACM), 22
Pogorelov, N. V., Borovikov, S. N., Kryukov, I. A., et al. 2017, J. Phys. Conf. Ser., 837, 012014
Pomoell, J., Kilpua, E., Verbeke, C., et al. 2017, in Proc. EGU General Assembly Conf. Abstracts, 19, 11747
Powell, K. G., Roe, P. L., Linde, T. J., et al. 1999, JChPh, 154, 284
Riley, P., Linker, J. A., & Arge, C. N. 2015a, SpWea, 13, 1
Riley, P., Lionello, R., Linker, J. A., et al. 2015b, ApJ, 802, 105
Riley, P., Mikic, Z., & Linker, J. A. 2003, AnGeo, 21, 1347
Riley, P., & Richardson, I. G. 2013, SoPh, 284, 217
Roussev, I. I., Galsgaard, K., Downs, C., et al. 2012, NatPh, 8, 845
Roussev, I. I., Gombosi, T. I., Sokolov, I. V., et al. 2003, ApJL, 595, L57
Schatten, K. H., Wilcox, J. M., & Ness, N. F. 1969, SoPh, 6, 442
Scherrer, P. H., Bogart, R. S., Bush, R. I., et al. 1995, SoPh, 162, 129
Schmieder, B., Aulanier, G., & Vrsnak, B. 2015, SoPh, 290, 3457
Schou, J., Scherrer, P. H., Bush, R. I., et al. 2012, SoPh, 275, 229
Schrijver, C. J., & DeRosa, M. L. 2003, SoPh, 212, 165
Schuck, P. W. 2008, ApJ, 683, 1134
Shen, F., Wang, Y., Shen, C., et al. 2017, SoPh, 292, 104
Shiota, D., & Kataoka, R. 2016, SpWea, 14, 56
Sokolov, I. V., van der Holst, B., Oran, R., et al. 2013, ApJ, 764, 23
Thernisien, A. F. R., Howard, R. A., & Vourlidas, A. 2006, ApJ, 652 763
Titov, V. S., & Demoulin, P. 1999, A&A, 351, 707
Titov, V. S., Torok, T., Mikic, Z., et al. 2014, ApJ, 790, 163
Török, T., Downs, C., Linker, J. A., et al. 2018, ApJ, 856, 75
Torok, T., & Kliem, B. 2005, ApJL, 630, L97
Torok, T., Kliem, B., & Titov, V. S. 2004, A&A, 413, L27
Toth, G., van der Holst, B., & Huang, Z. 2011, ApJ, 732, 102
Usmanov, A. V., & Goldstein, M. L. 2006, JGR, 111, A07101
Usmanov, A. V., Matthaeus, W. H., Breech, B. A., et al. 2011, ApJ, 727 84
van der Holst, B., Sokolov, I. V., Meng, X., et al. 2014, ApJ, 782, 81
Vandas, M., Fischer, S., Dryer, M., et al. 1996, JGR, 101, 15645
Vrsnak, B. 2001, SoPh, 202, 173
Vrsnak, B., & Gopalswamy, N. 2002, JGR, 107, 1019
Wang, A. H., Wu, S. T., Tandberg-Hanssen, E., et al. 2011, ApJ, 732, 19
Wang, Y.-M., & Sheeley, N. R., Jr. 1992, ApJ, 392, 310
Wang, Y.-M., & Sheeley, N. R., Jr. 1997, GeoRL, 24, 3141
Wang, Y. M., Ye, P. Z., Wang, S., et al. 2002, JGR, 107, 1340
Wu, S. T., Wang, A. H., Gary, G. A., et al. 2009, AdSpR, 44, 46
Yalim, M. S., Pogorelov, N. V., & Liu, Y. 2017, J. Phys. Conf. Ser., 837, 012015
Zhao, J., Couvidat, S., Bogart, R. S., et al. 2012, SoPh, 275, 375